Experimental demonstration of vanadium-doped nanostructured ceria for enhanced solar thermochemical syngas production

Experimental demonstration of vanadium-doped nanostructured ceria for enhanced solar thermochemical syngas production

Asim Riaz[a], Felipe Kremer[b,e], Tak Kim[c,e], Suchinda Sattayaporn[d,e], Takuya Tsuzuki[a], Wojciech Lipiński[a]*, Adrian Lowe[a]**

[a] Research School of Electrical, Energy and Materials Engineering, The Australian National University, Canberra, ACT 2601, Australia.

[b] Centre for Advanced Microscopy, The Australian National University, ACT 2601, Australia.

[c] School of Environment and Science, Griffith University, Nathan, Australia.

[d] Synchrotron Light Research Institute (Public Organization), Sirindhornwitchothai Building 111 University Ave., Muang District, Nakhon Ratchasima 30000, Thailand.

[e] Contributed equally.

* Corresponding author. *E-mail*: wojciech.lipinski@anu.edu.au; *Tel*: +61 2 612 57896

** Corresponding author. *E-mail*: adrian.lowe@anu.edu.au; *Tel*: +61 2 612 54881.

Abstract

Solar-driven thermochemical routes enable storage of solar energy in chemical form for off-sun use by means of synthetic fuel production. Here, we explore vanadium-doped ceria materials for partial oxidation of methane, followed by an efficient splitting of CO_2 and H_2O into syngas. The primary role of the dopant is to enhance and optimize the cycle capacity of ceria at low isothermal temperatures. The intake capacity of ceria lattice reached its saturation level with 5% of vanadium addition and further increase in V (%) forms a secondary phase ($CeVO_4$), which significantly affects the role of vanadium towards the syngas production performance enhancement. For instance, vanadium atoms migrate to the powder surface with V ≥ 5% and cause cracking of methane, while the lattice vanadium atoms (V < 5%) enhances the cycle capacity by providing reducing sites for the redox reactions and improve the oxygen mobility by inducing lattice distortions. The cycle capacity of V-doped ceria is four times higher than pure ceria, while the temperature for the methane partial oxidation reaction is decreased by up to 178°C with elevated

peak syngas production rates, after vanadium doping. The long-term redox activity of V-doped ceria materials for 200 cycles with up to 4.5 mmol g^{-1}/cycle of syngas is reported. This study demonstrates the concept of utilizing V-doped ceria to produce syngas *via* high temperature chemical looping reforming of methane and helps to strategically evaluate the redox materials as an efficient oxygen carrier for syngas production.

Keywords: Doped ceria, thermochemical, redox activity, sustainable fuels, thermogravimetric analysis, methane partial oxidation

I. Introduction

Environmental pollution has steered research towards renewable and sustainable energy and fuel resources. Synthetic fuels have emerged as one of the most suitable and sustainable alternatives to fossil fuels due to its low carbon footprint. Solar thermochemical processes have been extensively studied for the large-scale production of synthetic fuels via water and carbon dioxide splitting reactions, driven by renewable thermal energy, collected via solar concentrators.[1–7] Fast redox kinetics and high thermal stability of ceria make it the most widely utilized redox material for thermochemical processes. Despite these benefits, the low cycle capacity of ceria largely affects the yields of syngas during the reduction and oxidation reactions. Furthermore, sintering is another issue associated with nano-structured ceria, which results in a significant loss of surface area and slower redox kinetics. Substantial research efforts have been made to mitigate the above mentioned issues.[8–16]

Transition metal-doped ceria,[8,9,17–20] Ce-based binary and ternary compounds[10,21–24] and perovskite structures[23–25] have been considered to for improving the cycle capacity of ceria in thermochemical redox reactions. Beside small improvements in the oxygen exchange capacity, modified ceria structures often exhibit slow redox kinetics. Recently, many metal oxide

structures have been proposed as non-cerium-based alternative oxygen carriers.[9,26–33] However, numerous issues along with some advantages are reported during the redox cycling. For instance, despite fast reduction kinetics, perovskites often have slow and fractional reoxidation reactions. The initially fast and high oxygen exchange capacity of iron oxide drastically decreases after a few cycles due to sintering issues. In our previous study, the CeO_2–V_2O_5 binary phase systems (Reactions 1 and 2) have been shown to drastically enhance and stabilize redox kinetics and syngas yields during chemical looping dry/steam reforming of methane.[10,21] However, the redox mechanism of the independent vanadium ions inside the ceria lattice is yet to be explored.

$$2CeO_2 + V_2O_5 = 2CeVO_4 + \frac{1}{2}O_2 \quad (1)$$

$$CeVO_4 \underset{\text{Oxidation}}{\overset{\text{Reduction}}{\rightleftharpoons}} CeVO_3 + \frac{1}{2}O_2 \quad (2)$$

Here, reaction 1 shows the removal of oxygen during the solid-state reaction between CeO_2 and V_2O_5, while reversible formation of $CeVO_4$ phase results in the exchange of oxygen during reduction and oxidation reactions, (reaction 2). In addition, this oxygen exchange rotates the +4 (CeO_2) and +3 ($CeVO_4$) oxidation states of cerium during the redox reactions and enhances the cycle capacity. This mechanism drastically improved the syngas production yields by 68% when compared to pure ceria and a stagnant amount of H_2 (up to 220 mL g^{-1}) is produced during water splitting reactions.[10]

Here, we report a facile method for incorporation of vanadium into the ceria lattice. Methane partial oxidation (MPO) under continuous heating up to 1000°C is performed to find the lowest possible temperature for the peak syngas production rates and yields. Short (S) and long (L) cycles of CO_2 (MPO–CDS) and H_2O (MPO–WS) splitting reactions are performed to investigate the effects of vanadium doping on the syngas production performance of ceria. We

observed that vanadium doping lowers the reduction temperature and enhances the syngas production rates and yields for up to 200 continuous cycles. Structural study revealed that beyond the saturation level (i.e. 5% V), excess vanadium forms V_2O_5, which reacts with CeO_2 and results in a $CeVO_4$ phase. The vanadium present inside the ceria lattice and $CeVO_4$ presents a variety of redox mechanisms which significantly affects the thermochemical performances of V-doped ceria with vanadium content before and after the saturation levels. These findings are used to design and synthesize new materials with high thermochemical redox performance.

II. Experimental Procedures

2.1. Materials preparation

Nano-structured pure ceria (CeO_2) and *x*V-doped CeO_2 (*x* = 1%; 1VCe, 3%; 3VCe, 5%; 5VCe, and 7%;7VCe) powders were prepared by a facile liquid phase precursor decomposition method.[10,34] Briefly, different stoichiometric concentrations of cerium (III) nitrate hexahydrate (CeN_3O_9-$6H_2O$, Aldrich) and vanadium(V) oxytripropoxide ($C_9H_{21}O_4V$, Aldrich) were dissolved in ethanol, separately. Both solutions were then mixed and stirred at room temperature until a homogeneous sol was achieved. Finally, the sols were dried at 80°C and then fired at 900°C for 2 hr and ramp rate was set at 3°C min^{-1}.

2.2.Thermochemical cycling

A vertical-tube reactor placed inside an infrared gold image furnace (P4C-VHT, Advance Riko), was utilized to evaluate the pristine oxygen careers for thermochemical redox performance. The furnace was equipped with four infrared lamps and inner walls around the lamps are coated with thin layer of gold which act as an elliptical surface reflector, as shown in Figure 1. Powder samples were placed on a 2 mm thick layer of highly porous and high temperature resistant alumina-based

fibrous wool (97% Al_2O_3 and 3% SiO_2), placed axially in the middle. Another layer of fibrous wool was inserted into the tube and placed 1 cm above the powders to avoid the powder displacement caused by gas flow. Gas flow rates were regulated by flow controllers (F201CV, Bronkhorst) and pneumatically actuated valves (1315R, Swagelok). A B-type thermocouple sealed in an alumina sheath was inserted in the tube to monitor sample temperature during the redox reactions. The tube outlet was attached to a quadrupole mass spectrometer (OmniStar^{TM} GSD 320, Pfeiffer Vacuum) to record the composition of product gases.

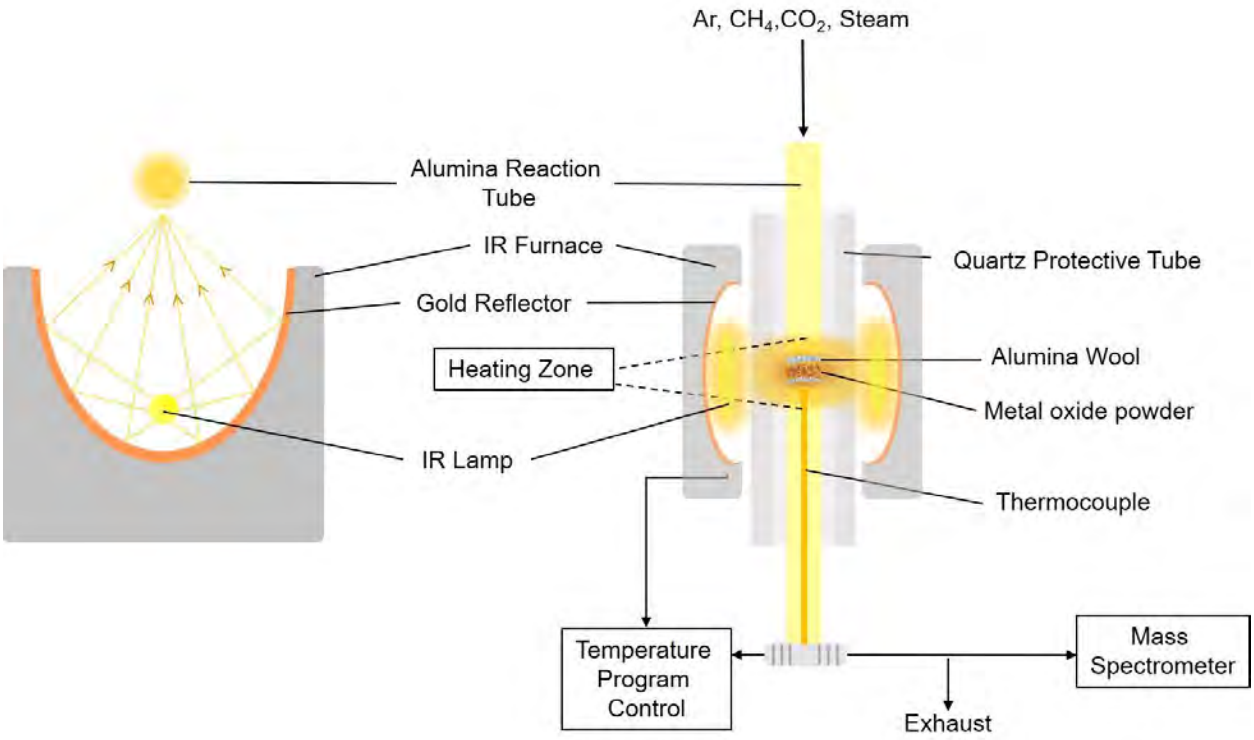

Figure 1. Schematic diagram of thermochemical testing setup: (Left) Cross section of the IR furnace showing the light reflecting on the elliptical surface towards the alumina reactor tube. (Right) Schematic diagram showing the tubular reactor set-up utilized for the thermochemical redox experiments, mass-spectrometer for gas analysis and the temperature program controller to set and monitor the temperature.

Ar gas (Ar grade 5.0) was purged in the tubular reactor with a flow rate of 500 mL min^{-1} between every reduction-oxidation reaction and during the heating/cooling steps. The reactor was

heated to an optimized isothermal temperature of 900°C at a ramp of 100 °C min^{-1}. Powder samples were reduced in a flow rate of 20 mL min^{-1} CH_4 (grade 4.5), while re-oxidized by 10 mL min^{-1} CO_2 (grade 4.5) flow. For WS reactions, steam vapor was generated at 95°C in a bubbler filled with DI water. The vapors were carried by flowing Ar through the bubbler with a flow rate of 30 mL min^{-1}, which was further diluted by Ar with 220 mL min^{-1} flow rate. Total gas flow rate was kept constant at 250 mL min^{-1} during each reduction and oxidation reaction.

2.3.Materials Characterization

Pristine and after redox cycling samples were characterized by the following techniques. A field emission scanning electron microscope (FESEM, Ziess Ultraplus) was utilized to observe the morphology of the powder samples. Powders were dispersed on carbon tape and placed on the top of a sample holder. A high-resolution transmission electron microscope (HR-TEM, JEOL 2100F) was utilized to estimate the particle size distribution and to measure lattice spacing. Energy dispersive spectroscopy (EDS) analysis was carried out by the scanning transmission electron microscopy (STEM-EDS) technique. TEM samples were prepared by drop casting the powder dispersion (in ethanol) onto lacy carbon-coated 200 mesh Cu grids. Image processing and particle size/lattice planar spacing measurements were done using ImageJ software.

Atomically resolved estimation of lattice spacing and the positions of Ce and V atoms was carried out via electron energy loss spectroscopy (EELS) technique by utilizing a Hitachi HF500 Cs-STEM/TEM instrument equipped with a W (310) cold-cathode FEG electric field filament and a Cs probe STEM corrector. The accelerating voltage was set at 200 kV for the high-resolution imaging and EELS analysis.

A D2 phaser diffractometer (Bruker) was utilized to carry out the phase and structural determination of the powder samples via X-ray diffraction (XRD) technique. The instrument was equipped with a Cu Kα (1.54Å) radiation source operating at 30 kV voltage and 10 mA current. XRD patterns were recorded at a scan rate of 0.75° min^{-1} in the Bragg's angle 2T range of 10–80° incrementing by 0.02° per data point. Match3 V.3.8.1.143 (Crystal Impact) software was utilized for phase identification, while Rietveld refinement method was applied on the XRD patterns for phase quantification.

Chemical analysis of powder surfaces was carried out by utilizing a Thermo Fisher ESCALAB 250 Xi X-ray photoelectron spectrometer (XPS). The instrument was equipped with a microprobe and an aluminum Kα radiation source with a spot size of 200–900 μm operated at 15 kV voltage and a current of 12 mA. Samples were scanned at different spots with an energy range of 160–40 eV, depending upon the sample behavior and desired resolution. Spectra were deconvoluted by using Advantage software v5.978 (Thermofisher). The C 1s peak of advantageous carbon at 284.8 eV was used as a reference for the binding energies obtained in the survey spectra.

Information about the Ce L3 and V K edges was obtained from the X-ray absorption spectroscopy (XAS) technique in the X-ray absorption near edge structure (XANES) region. The spectra were obtained in transmission and florescence modes at BL5.2 of Synchrotron Light Research Institute (SLRI), Thailand. Electron beam energy was 1.2 GeV and current ranged from 80 to 150 mA, while the maximum photon flux was $1.1–1.7\times10^{11}$ photons.s^{-1}. Two germanium (220) single crystals were utilized as a monochromator for an X-ray beam size of 14 mm (width) and 1 mm (height) with a spatial resolution of 0.2 eV. The normalized XANES spectra were processed and analyzed on Athena software.

Structural analysis of oxygen carriers was performed on a Raman imaging microscope (Renishaw plc, model 2000) equipped with an Olympus BH2 microscope, a motorized XYZ stage, an air-cooled CCD detector and a CCD camera. A 785 nm NIR laser source was used to excite the powders and spectra were recorded in a Raman shift range of 100–1200 cm^{-1}. Powders were exposed to the laser power, adjusted between 0.01 to 0.5% (<6 MW) for 20 s.

Thermogravimetric analysis (TGA) and differential thermal analysis (DTA) were performed (NETZSCH STA 449 F3 Jupiter). Twenty consecutive isothermal MPO–CDS redox cycles were performed to measure the mass change and enthalpy of reduction and oxidation reactions. Operating conditions such as temperature, reducing and oxidizing gases, and duration were similar to the experiments performed in the IR furnace. However, the gas flow rates for CO_2 and CH_4 were kept constant at 10 mL min^{-1} and Ar as carrier gas with a flow rate of 125 mL min^{-1}. The furnace was heated with a ramp rate of 20 °C min^{-1}.

III. Results

3.1. *x*$VCeO_2$ materials before redox cycles

FESEM analysis revealed initial morphological information about the pristine *x*$VCeO_2$ nanostructures. The average particle size increased from 18 ± 5 nm in pure nano-ceria to 38 ± 6 nm after 7% of vanadium addition, and a porous network of nanoparticles was observed with vanadium addition (Figure SI 1). Figure 2a shows particle distribution in the ceria nanopowders doped with 3% vanadium, where estimated average particle size of 20 ± 5 nm is observed. The vanadium incorporation also caused lattice distortion in the ceria structures and the lattice spacing increased from 0.125 nm in pure nanoceria to 0.145 nm in 5$VCeO_2$ nano powders. However, vanadium contents greater than 5% lowered the lattice spacing, due to the possible vanadium saturation in the CeO_2 lattice and segregation of the $CeVO_4$ phase (Reaction 1).

EELS spectra measured from the respective high-angle annular dark-field (HAADF) image (Figure 2b), showed the major edges of vanadium, cerium and oxygen elements (Figure 2c). The major edges of cerium Ce O2 at 15 eV, Ce N at 120 eV, Ce M5 at 883 eV and Ce M4 at 901 eV indicated high cerium (IV) concentrations in the CeO_2 lattice.[35] Major edges of vanadium, V L2 at 529 eV and V M2 at 38 eV confirmed the presence of V^{5+} in the CeO_2 lattice, (Figure 2c).[36]

Figure 2e present the elemental distribution of vanadium in the pristine $3VCeO_2$ nano powders. The EDS spectra acquired at different spots on the grey scale image (Figure 2d) of $3VCeO_2$ powders are shown in Figure 2f. Distinct elemental energy peaks of Ce and V in the EDS spectra confirmed the vanadium presence along with the cerium and oxygen elements.

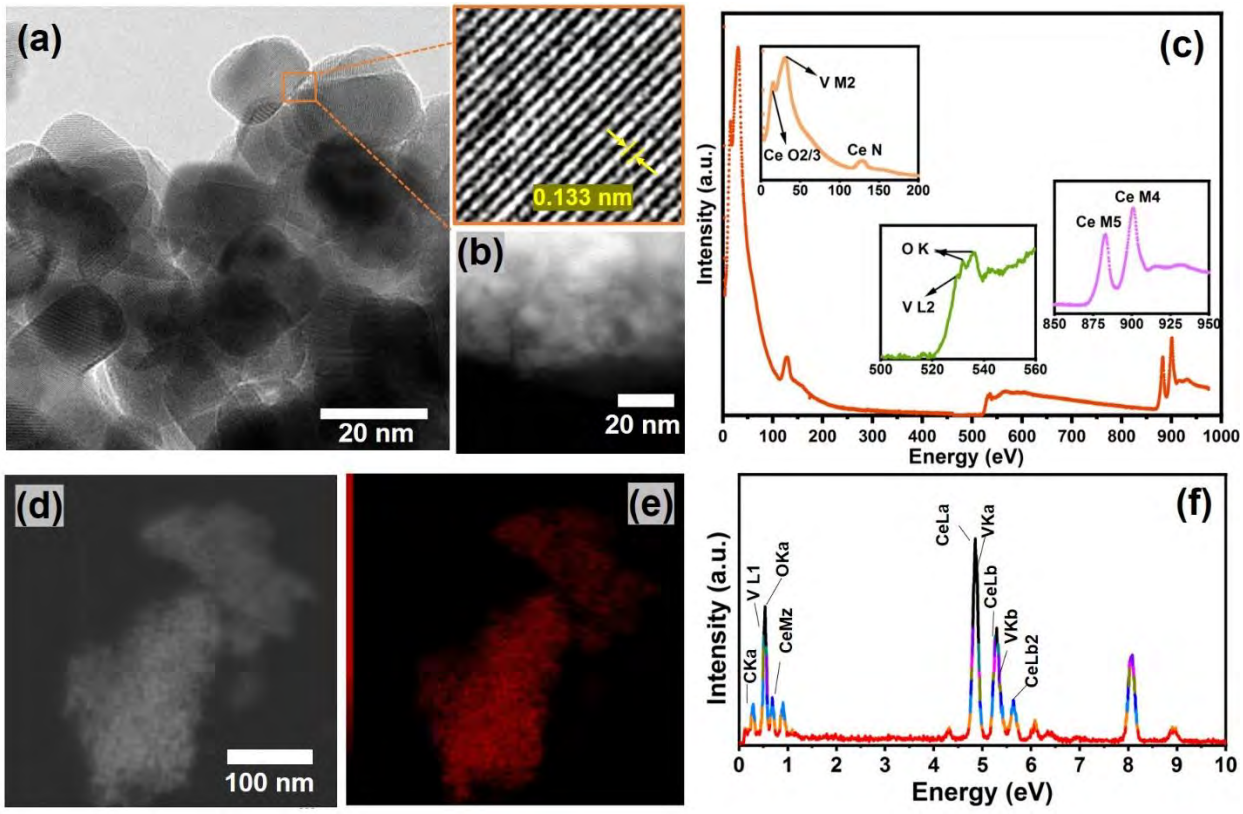

Figure 2. Morphological and chemical analysis of pristine $xVCeO_2$ materials: (a) HR-TEM micrograph showing the particle size distribution in the $3VCeO_2$ sample. An expanded section from the image shows the inner lattice spacing. (b) HAADF image of the $3VCeO_2$ sample. (c) EELS spectra containing information about Ce O2,3, Ce M4, Ce M5, O K, V L2 and V M2 edges in the $3VCeO_2$ sample. STEM-EDS maps of (e) vanadium

(red) corresponding to the (2d) grey scale image of 3VCeO$_2$ sample. (f) EDS spectra measured from the grey scale image shown in part 2d.

XRD analysis provided information about changes in the ceria structure such as Bragg's angle shift, lattice spacing and phase segregation. Figure 3a shows the XRD patterns for pristine *x*VCeO$_2$ nano powders. A triclinic CeO$_2$ crystal structure was confirmed from the pure ceria XRD pattern. Vanadium doping below 5% showed a slight 2θ shift and phase quantification revealed a 100% CeO$_2$ phase. However, further addition exceeded the saturation limit of vanadium in the CeO$_2$ lattice and promoted the formation of CeVO$_4$ phase, as described in Reaction 1.[10,37] Figure 3b shows the evolving CeVO$_4$ phase, as the XRD peak intensity at ~25° increased in 7VCeO$_2$ powders. Figure 3c presents changes in the lattice spacing and CeVO$_4$ phase concentration in CeO$_2$ nano powders with vanadium addition. Considerable amounts of approximately 8.2% of CeVO$_4$ phase were observed after 7%V addition to the CeO$_2$ nano structures.

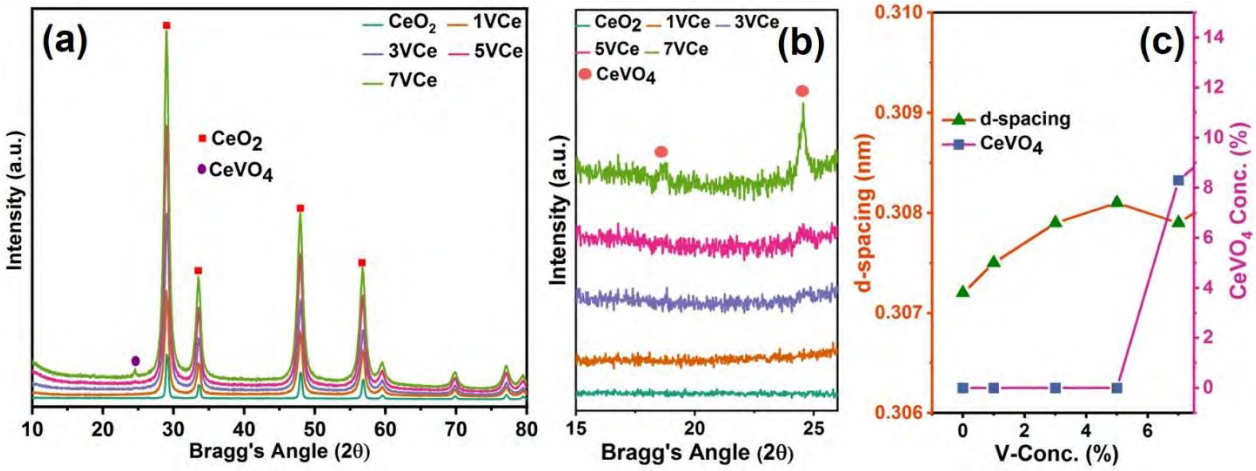

Figure 3. Structural characterization of pristine V-doped ceria nano structures (a) XRD patterns of pristine *x*VCeO$_2$ materials. (b) Evolution of CeVO$_4$ phase with the addition of vanadium in ceria. (c) Variations in d spacing and CeVO$_4$ concentrations as a function of vanadium content.

Further analysis performed using the Raman technique evaluated the structural changes induced by vanadium doping into the CeO_2 nano structures. Figure 4a compares the Raman spectra of V-doped ceria powders with the pure CeO_2 and V_2O_5 used as reference. Vanadium doping slightly shifted the CeO_2 peak at 461.87 cm^{-1} towards low Raman frequencies.[38,39] Raman shift peaks at 861.25, 799.21, 787.84, 379.54, and 259.19 cm^{-1} confirmed the formation of $CeVO_4$ phase in the V-doped ceria powders with vanadium content greater than 5%.[37,39,40]

To gain insights into the effects of vanadium doping on the surface chemical composition, the V-doped ceria nano powders were investigated by XPS analysis. Figures 4b–4d present the photoemission spectra of O 1s, Ce 3d and V 2p measured on pristine 1, 3, and 7% V-doped ceria powder surfaces. The oxygen O 1s spectra were fitted into three different components: The first peak (OI) situated at 529.3 eV is associated with the lattice oxygen; the second peak (OII) at ~530.1–531.2 eV corresponds to the oxygen atoms situated near the vacancy-rich regions; the third peak (OIII) at 532.6 eV is ascribed to the physiosorbed H_2O or –OH species. The lattice oxygen O1 peak shifted towards higher binding energies, depicting stronger M–O bonds due vanadium incorporation in the CeO_2 lattice, as compared to that in the pure CeO_2 structures.[41] The oxygen leaching in Reaction 1 resulted in higher concentrations of the OII species in the 7VCe sample compared to that of xVCeO$_2$ with x = 1–5 %. The Ce 3d spin-orbital split multiplet of CeO_2 mostly remained unchanged after vanadium doping (Figure 4c). However, the intensity of the 3d 3/2 peak at 917 eV decreased in the 7VCe sample due to the presence of Ce^{3+} in the growing $CeVO_4$ phase. In addition, strong V 2P 3/2 and 5/2 peaks in the 7VCe sample characterizes vanadium onto the surface of ceria nanopowders (Figure 4d).

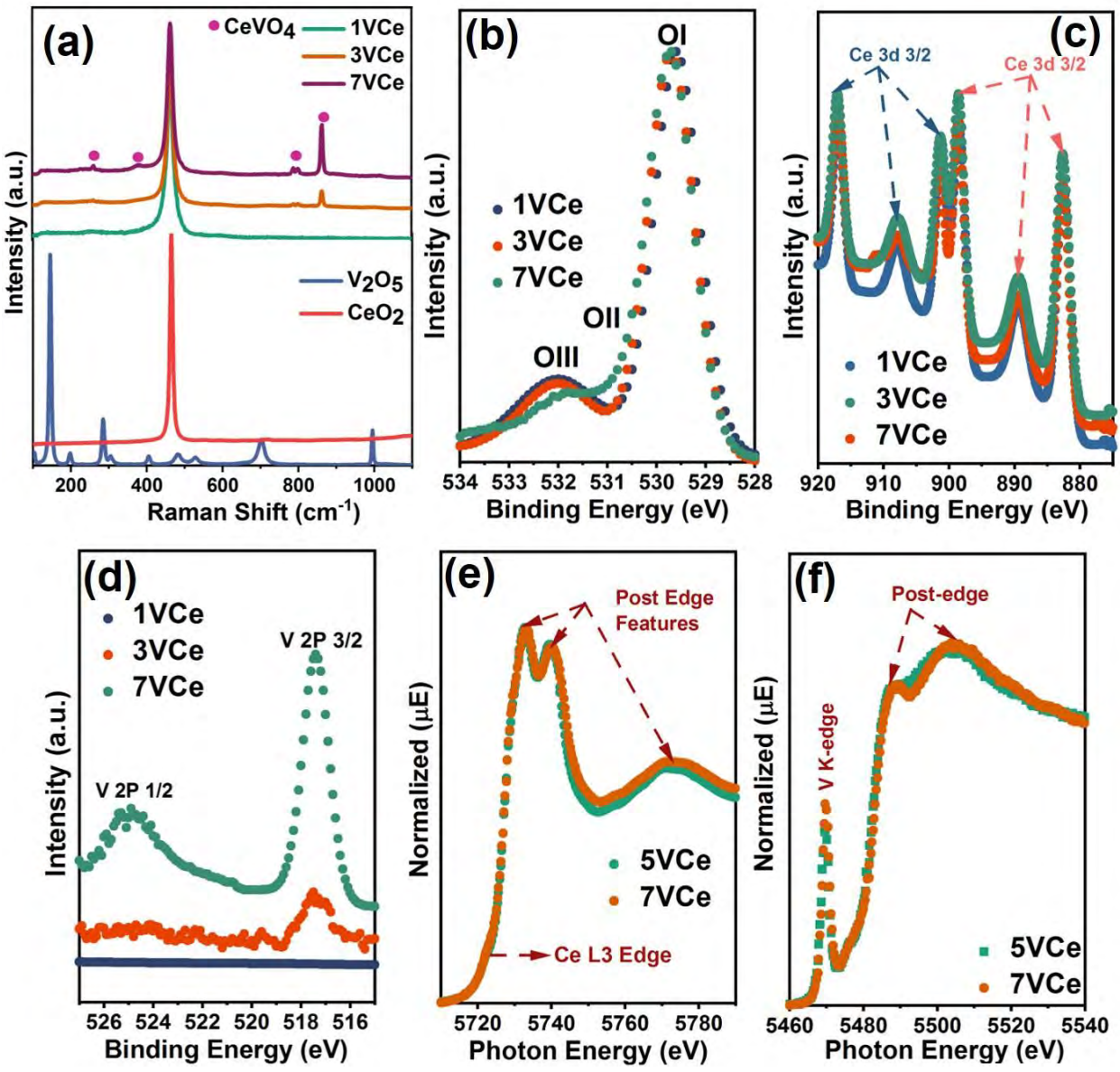

Figure 4. Structural and surface study of pristine *x*VCeO$_2$ materials: (a) Raman spectra with information about the evolution of the CeVO$_4$ phase with V addition in CeO$_2$ structures along with the spectra of reference pure CeO$_2$ and V$_2$O$_5$ samples. XPS spectra measured from (c) Ce 3d and (d) V 2P spin orbitals in *x*VCeO$_2$ materials with variable vanadium concentrations. XANES spectra of (e) Ce L3 and (f) V K edges in 5VCe and 7VCe samples.

Photon energy spectra of Ce L3 and V K edges were obtained from ex-situ XANES analysis of V-doped CeO$_2$ powder samples, (Figures 4e and 4f). The oxidation states of Ce and V were calculated by comparing the acquired photon energy data with cerium and vanadium oxide

standard samples (Figure SI 2). The Ce L3-edge energy for pure and V-doped CeO_2 was recorded at 5727 eV and the calculated cerium oxidation state (+4) also remained unchanged due to the dominating CeO_2 phase (Figure 3e). The $CeVO_4$ phase growth in the 7VCe sample results in a slight shift of the vanadium K-edge to higher energies (5483.0 eV) and the calculated positive charge on vanadium was also increased to +5.1, (Table T1 and Figure 4f). Low intensities of the pre-edge absorption feature at 5469.79 eV confirmed the XPS findings on high oxygen concentrations near vacancy-rich regions in the 7VCe sample.[42] This also refers to the formation of V–O bond cluster in $CeVO_4$ phase.

3.2. Thermochemical performance: MPO activation temperature

Multiple aspects of thermochemical performance of the pristine *x*$VCeO_2$ including MPO activation temperature, fuel production rates and yields were evaluated. The MPO activation temperature experiment was performed by heating the powder samples from ambient temperature to 1000°C with a ramp rate of 3°C min^{-1} in a CH_4 atmosphere. Figure 5a shows the spontaneous H_2 production rates produced by *x*$VCeO_2$ powders during reduction. The recorded temperature for the peak H_2 rates (0.33 mmol min^{-1} g^{-1}) produced by pure ceria was 964.36 °C. Vanadium addition significantly reduced the temperature for its peak syngas production rates (Figure 5b) where only 1%V resulted in the peak production rates of H_2 (0.57 mmol min^{-1} g^{-1}) and CO (0.23 mmol min^{-1} g^{-1}), at 883.69 °C. Highest rates of H_2 (0.6 mmol min^{-1} g^{-1}) and CO (0.17 mmol min^{-1} g^{-1}) were achieved at the lowest temperature of 785.35 °C with 5%V doping. The rates of partial oxidation of methane were significantly slower than the thermal cracking of methane. Thus, the recorded instantaneous H_2 rates were much higher than that of CO.

Activation of the MPO reaction was further investigated by TGA/DTA analysis. Samples were heated from ambient temperature to 1000 °C at a ramp rate of 3° min^{-1}, while the methane

flow was kept constant at 10 mL min^{-1} with 115 mL min^{-1} Ar as carrier gas. The spontaneous mass change was recorded as a function of temperature, simulating the gas production rates shown in Figure 5a. Evidently, the mass loss in pure ceria started at higher temperatures when compared to that of V-doped ceria samples. The mass loss in 5VCe powder was maximum with the lowest recorded temperature (Figure 5c), which is in line with the results obtained in Figure 5a. Considering the temperature variance, an optimized temperature (i.e. 900°C) was set to further investigate pure and V-doped ceria powders for MPO–CDS and MPO–WS redox cycles.

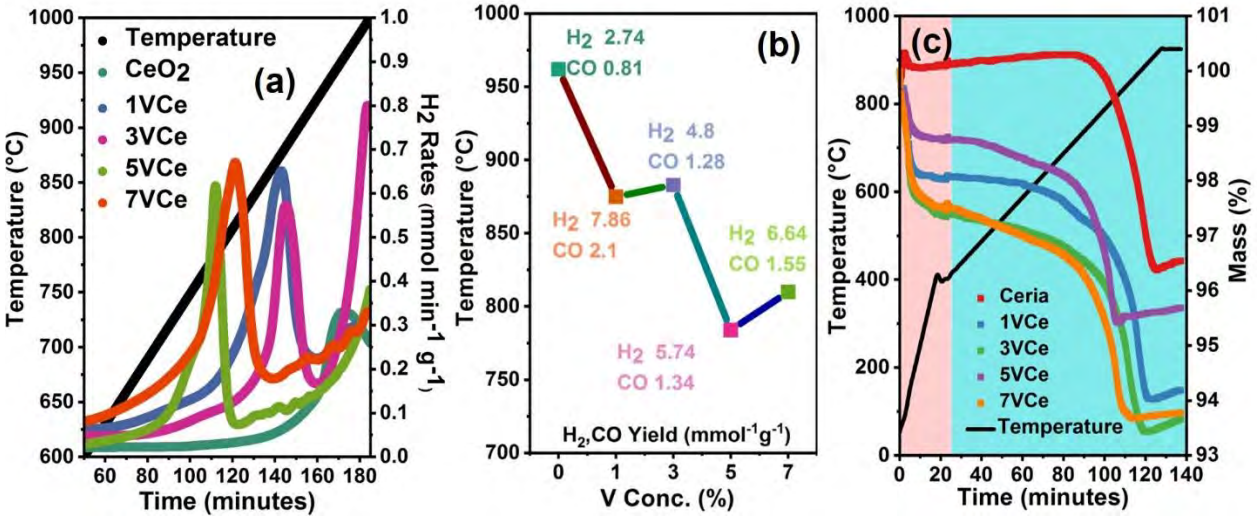

Figure 5. Effects of vanadium doping on the activation temperature for the methane partial oxidation reaction: (a) H_2 evolution profiles of *x*$VCeO_2$ samples during constant heating from RT to 1000°C in CH_4 atmosphere. (b) Peak H_2 and CO rates at temperatures achieved by pure and V-doped ceria powders. (c) TG mass variance in *x*$VCeO_2$ samples during the continuous heating from RT to 400°C in Ar and from 400°C to 1000°C in CH_4 atmosphere.

The mass change (Δm%) during three preliminary MPO–CDS redox cycles is presented in Figure 6a. The Δm (%) in pure ceria powders decreased to half after the first cycle, while doping of vanadium significantly enhanced and stabilized the mass change. The recorded mass change and enthalpy of reactions for 3VCe samples during 20 consecutive MPO–CDS cycles are presented in Figure 6b. Clearly, stable mass change and enthalpies are observed without significant changes

after the first few cycles. The expanded view of TGA and DTA graph for cycles 14th to16th presents a clear image of mass change and enthalpy during the MPO–CDS redox cycles (Figure 6c and 6d).

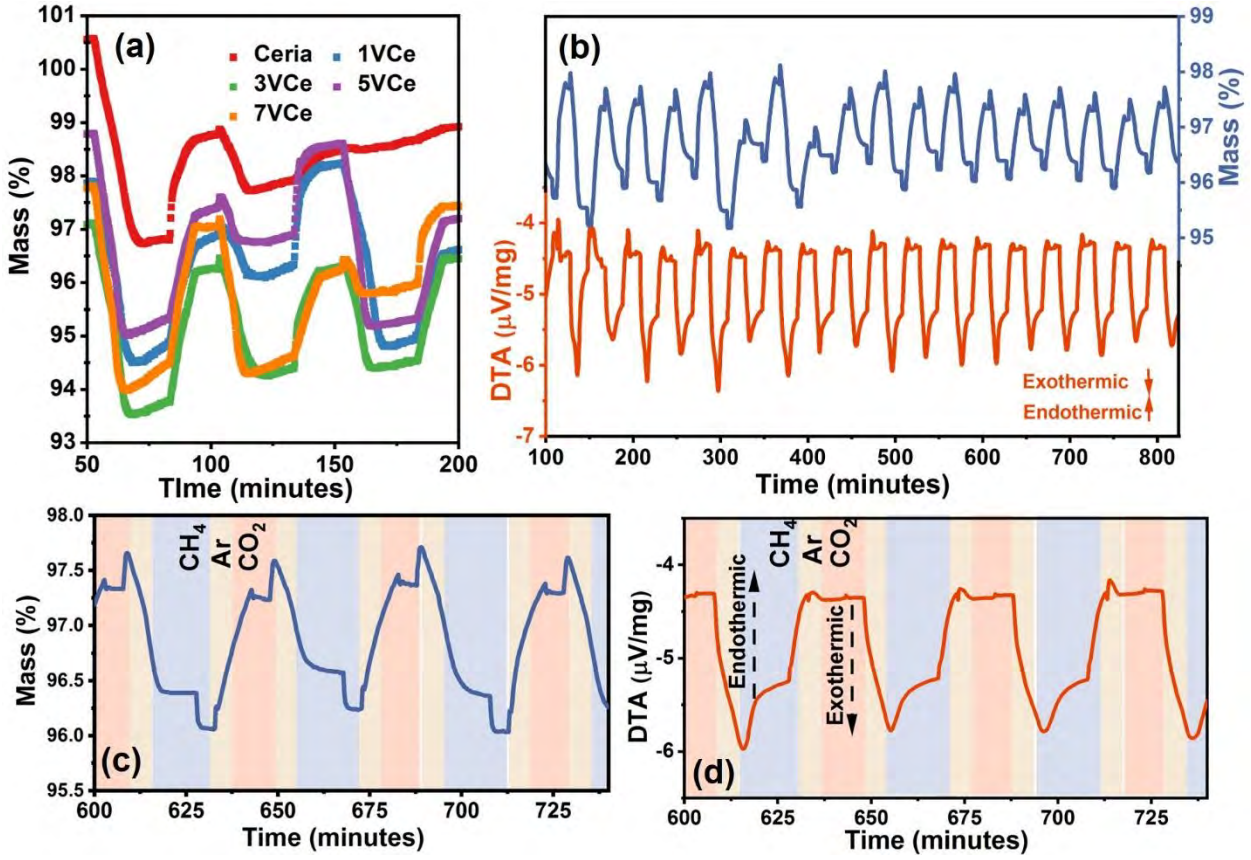

Figure 6. Thermogravimetric analysis of V-doped ceria nano powders. (a) TG mass change (%) in *x*VCeO$_2$ powders during three consecutive MPO–CDS redox cycles. (b) TGA and DTA analysis of 3VCeO$_2$ samples for 20 consecutive MPO–CDS redox cycles. Expanded view of (c) TGA and (d) corresponding DTA signals for cycles 14th to 16th.

The syngas production performance of V-doped CeO_2 nano structures were further evaluated for partial oxidation of methane coupled to CO_2 and H_2O splitting reactions, in sections 3.3 and 3.4. The production rates/yields, fuel selectivity, H_2/CO ratios and carbon contents were evaluated as a function of reaction time, where the duration of reduction and oxidation reactions was altered to study the redox potential of materials during MPO, WS and CDS reactions. The first set of experiments, referred as short (S) cycling, consist of a 20 min material reduction (MPO)

followed by a 10 min reoxidation (WS or CDS) reaction. The duration of reduction and oxidation reactions was increased to 90 min 70 min, respectively and referred as long (L) cycling. In the following figures and discussions in the text and SI, the short redox cycles will be referred to as S/MPO–CDS and S/MPO–WS, while the L/MPO–CDS and L/MPO–WS will be used to refer to the long redox cycles.

3.3. MPO–CDS cycling

The syngas production rates improved with vanadium doping in ceria. The highest production rates for H_2 (2.8 mmol min^{-1} g^{-1}) and CO (1.32 mmol min^{-1} g^{-1}) were achieved by 1VCe powders during the S/MPO reaction, which was 4 times higher than that of pure ceria and 3 times higher than pure $CeVO_4$ (Figures 7a and 7b). Notably, the syngas production rates with a spike at the end of the MPO reaction in Figure 7a is similar to that observed in the TG curve (Figure 6b) with an abrupt mass decrease. Further increases in the vanadium content showed up to a 200% increase in syngas production rates compared to pure ceria (Figure SI 3a and SI 3b). The 1VCe sample produced the highest rates of CO up to 1.25 mmol $min^{-1}g^{-1}$, during the CO_2 splitting reaction. Overall, all the *x*$VCeO_2$ materials showed enhanced syngas production performance compared to pure ceria and $CeVO_4$, during the S/MPO–CDS redox cycles.

Syngas yields produced by the *x*$VCeO_2$ powders during S/MPO–CDS cycles are presented in Figure 7c. The highest yields of H_2 (18.5 mmol g^{-1}) and CO (8.1 mmol g^{-1}) were achieved with the 1VCe sample upon reduction, while, 6.8 mmol g^{-1} of CO were produced during the CO_2 splitting reaction. A decline in the syngas yields was observed in the 3VCe and 5VCe samples. This may be due to the saturated vanadium atoms impeding the oxygen exchange in the ceria lattice. The 1VCe sample demonstrated a high CO selectivity (SCO) of 96.58% and H_2/CO ratio of 2.1 with only 0.1153 mmol/g of deposited carbon, during the S/MPO–CDS redox cycles, Figure

7d. However, despite high oxygen ion conductivity, ceria produced the largest amounts of deposited carbon due to its low cycle capacity.

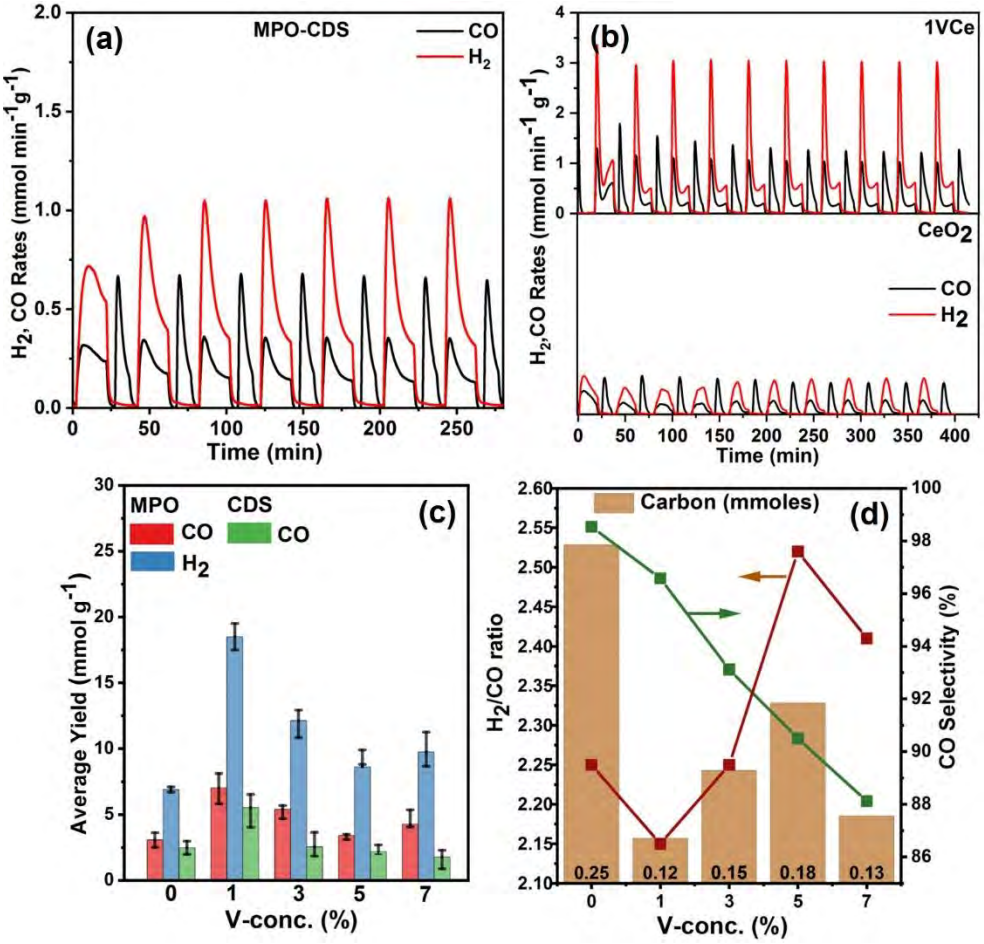

Figure 7. Thermochemical syngas production performance during S/MPO–CDS redox cycles: (a)CeVO4. (b) Syngas production rates comparison between pure ceria and the 1VCe sample, (c) average syngas yields and (d) H_2/CO ratios, CO selectivity and deposited carbon moles as a function of vanadium concentration in CeO_2 powders.

The 7VCeO_2 powders produced the highest average rates of H_2 (11 mmol min^{-1} g^{-1}) and CO (2.5 mmol min^{-1} g^{-1}) during the L/MPO reaction while CO yields of up to 2.5 mmol $min^{-1}g^{-1}$ were recorded during the L/CDS reaction (Figure 8a). Long reductions enhanced the oxygen exchange, possibly due to the migration of saturated vanadium atoms from the lattice to the surface

of the ceria particles. High $CeVO_4$ contents in the xVCeO$_2$ powders after the L/MPO–CDS cycles supported this suggestion.

Prolonged reduction and oxidation reactions significantly affected the syngas yields during the L/MPO–CDS redox cycles (Figure 8b). The 7VCe sample produced the highest yields of H_2 (117 mmol g^{-1}) and CO (35 mmol g^{-1}) during the L/MPO reaction, while the re-oxidation resulted in 57 mmol g^{-1} of CO (Figure 8b). This contrasts with the data recorded during the S/MPO–CDS redox cycle and will be discussed in the post-cycling structural study and the discussion section. Pure ceria produced a substantial amount (0.41 mmol/g) of deposited carbon, which decreased significantly with vanadium content. In addition, the H_2/CO ratio also decreased from 4.25 in pure ceria to 2.52 in the 1VCe sample (Figure 8c).

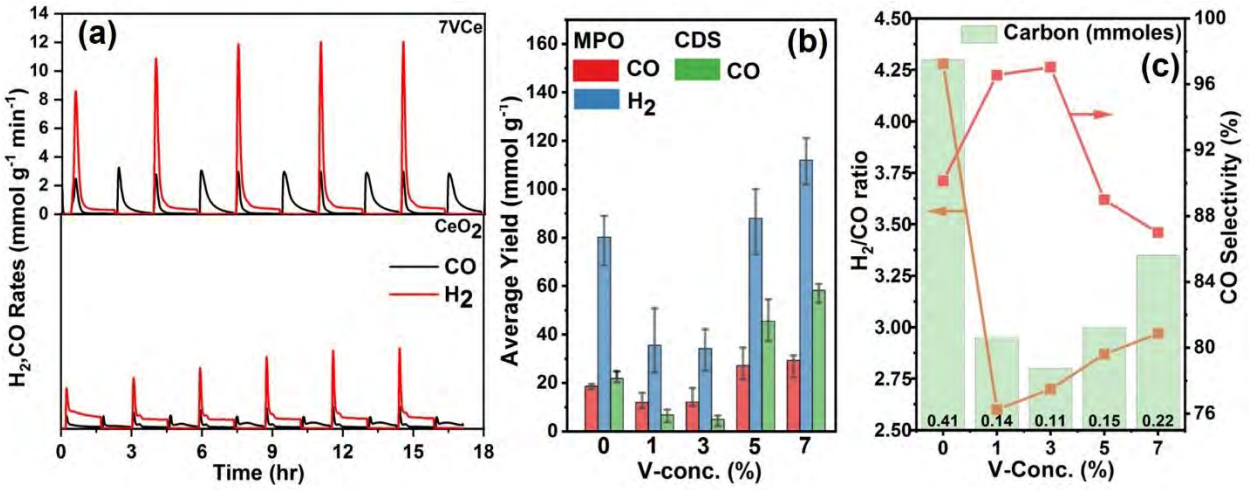

Figure 8. Thermochemical syngas production performance during L/MPO–CDS redox cycles: Comparison of syngas production (a) rates and (b) yields by pure ceria and V-doped ceria powders. (c) Change in H_2/CO ratios, CO selectivity and deposited carbon moles with various vanadium concentrations.

3.4. MPO–WS cycling

The reoxidation potential of xVCeO$_2$ materials was evaluated during S/MPO–WS and L/MPO–WS redox cycles. Water splitting reactions significantly affected the MPO reaction rate

profiles, where the rates of chemical looping methane reforming reaction rose exponentially, after a period of slow reaction rates (Figure 9a).

Syngas production rates and yields drastically increased with V-doped ceria, during the S/MPO–WS and L/MPO–WS redox cycles. Figure 9a shows higher and more stable syngas rates produced by the V-doped ceria samples when compared to that of pure ceria. In addition to the V-doped ceria nanostructures, pure $CeVO_4$ powders also showed significantly improved and stable syngas production rates than that of pure CeO_2 powders, yet not the highest, (Figure SI 4). The average syngas production rates from the 7VCe samples were the highest with 0.67 mmol min^{-1} g^{-1} of H_2 and 0.29 mmol min^{-1} g^{-1} during the S/MPO reaction while reoxidation by the water splitting reaction resulted in 0.22 mmol min^{-1} g^{-1} of H_2 (Figure 9b). The yields of H_2 and CO produced by 7VCe sample were 12.8 mmol g^{-1} and 5.85 mmol g^{-1}, respectively, during the S/MPO reaction. The amount of H_2 (1.9 mmol g^{-1}) produced during the H_2O splitting reaction was twice that produced by pure ceria (Figure 9c). Significant improvements in the purity of the H_2 and H_2/CO ratio were observed after vanadium doping of ceria. The purity of H_2 varied from 76% in pure ceria to 95% after V-doping (Figure 9d). The oxidation of carbon species by H_2O significantly slowed down the powder's reoxidation and resulted in low H_2 yields and low H_2 purity. High vanadium contents and pure ceria showed high H_2/CO ratios and elevated amounts of carbon content and the oxidation of surface carbon was prominent in the L/MPO–WS redox cycles (Figure 9e). However, this also resulted in relatively lower H_2 yields from the H_2O splitting reactions compared to that from S/MPO–WS cycling (Figure 9f).

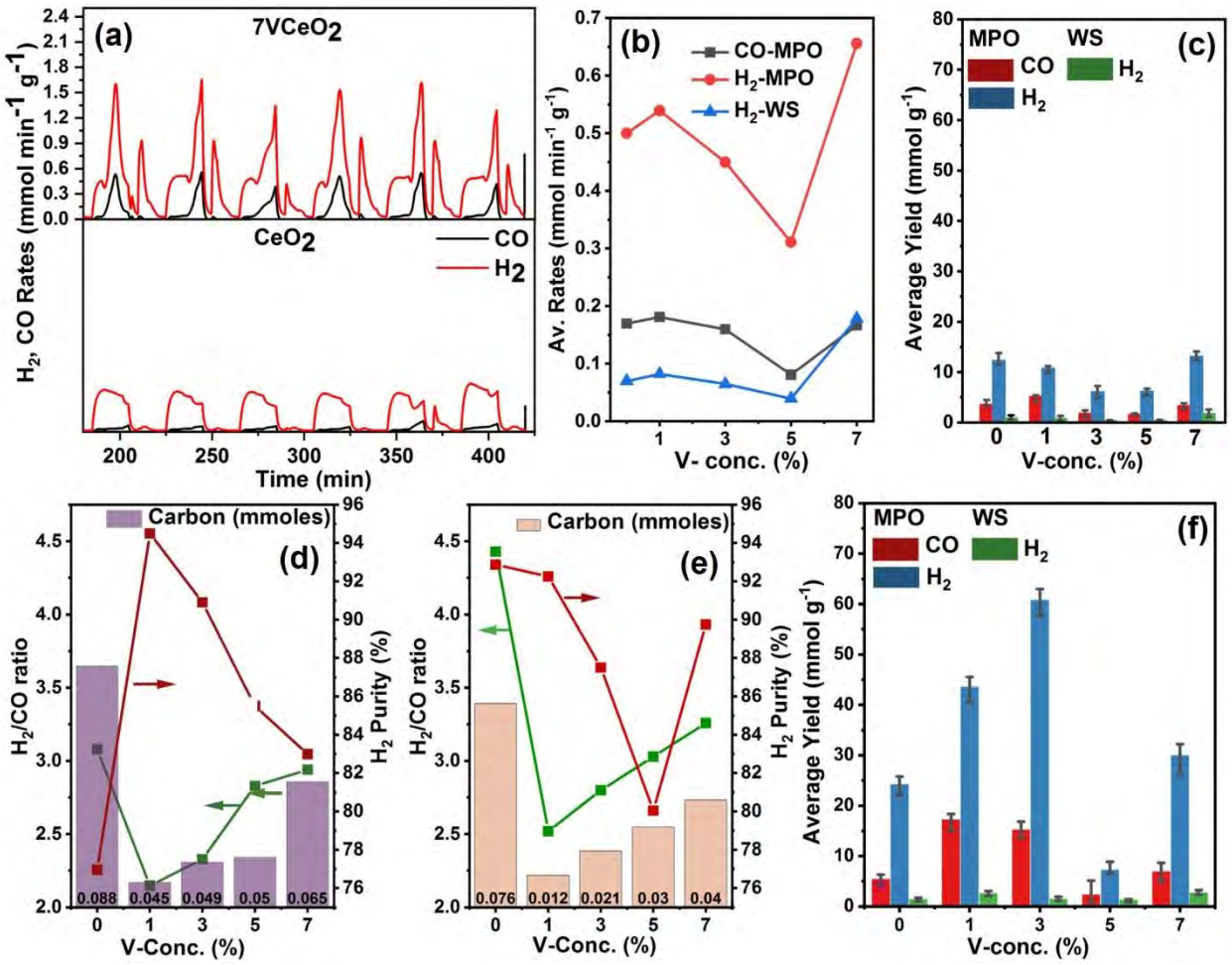

Figure 9. Thermochemical syngas production performance during MPO–WS redox cycles: (a) Comparison of the average syngas production rates between pure ceria and the 7VCe sample during S/MPO–WS redox cycles. (b) Average syngas rates produced by $xVCeO_2$ samples. (c) Average yields of syngas and (d) H_2/CO ratios, purity of H_2 and carbon contents recorded during S/MPO–WS redox cycles. (e) H_2/CO ratios, purity of H_2 and carbon contents and (f) average syngas yields, recorded during the L/MPO–WS redox cycles.

3.5.Post cycling material study

Cyclic redox reactions carried out at high temperatures resulted in the sintering of nano powders, which indirectly affected the thermochemical redox performance by hindering the solid-gas transfer. The durations and temperatures of cycles greatly influenced the extent of sintering. For instance, large particles are observed after high temperature reduction and long redox cycles as compared to those in short duration cycles being carried out at 900°C (Figure SI 5).

The X-Ray diffraction technique was utilized to study the structural and phase changes in the pure nano ceria and V-doped ceria nanostructures after redox cycling. Reduction of xVCeO$_2$ nanostructures resulted in a simple non-stoichiometric oxygen exchange in ceria (Figure 10a). The diffraction peaks of the $CeVO_4$ phase disappeared after its reduction to the $CeVO_3$ phase (Reaction 2), which was recovered upon the reoxidation reactions.[43,44] Higher concentrations of $CeVO_4$ phase were observed after the L/ MPO–CDS cycles when compared to that of S/MPO–CDS cycles. The deposited carbon during the prolonged exposure to the carbonaceous atmosphere caused slow oxygen exchange to the ceria lattice. Instead, the surface vanadium and cerium species were reoxidized and formed the $CeVO_4$ compound, after the removal of surface carbon. Another possible reason for the high $CeVO_4$ phase may be the prolonged oxidation of surface carbon, which eased up the oxygen exchange for the reoxidation reactions. The considerable amounts *c.a.* 13.9% of $CeVO_3$ along with the 7.6% $CeVO_4$ phase in 7VCeO$_2$ powders showed the partial reoxidation of the $CeVO_3$ phase during the L/MPO–CDS cycles.

The water splitting reactions facilitated the cyclic $CeVO_4$ concentrations due to the low deposited carbon contents, as compared to that of S/MPO–CDS and L/MPO–CDS redox cycles. Small amounts (5%) of $CeVO_4$ were also observed in the 5VCeO$_2$ powders after the MPO–WS cycles, which indicates the escape of vanadium from the ceria lattice to the surface of ceria nanoparticles. This depicts faster rates for Reaction 2 on the surface compared to that of non-stoichiometric reoxidation of reduced pure ceria nanostructures. However, the unsaturated vanadium content improved the rates and cycle capacity of ceria by inducing lattice distortions due to variable cationic radius and the V^{+5} cations draw more oxygen species into the ceria lattice.

The deposited carbon was investigated by the EDS technique after the reduction and reoxidation reactions. A green color STEM-EDS map shows carbon content on the reduced

$5VCeO_2$ powders (Figures 10b and 10c). The EDS spectra show the higher intensity counts of the C Kα peak in reduced samples, when compared to those from the oxidized samples. In addition, the powder surfaces covered with carbon also lowered the intensities of other elements present in the reduced $5VCeO_2$ powders (Figure 10d).

Figures 10e and 10f show the changes in the surface oxygen species induced by cyclic oxygen exchange during the reduction and re-oxidation reactions. Low OI-to-OII intensity ratios pointed to oxygen removal and increased numbers of oxygen vacancies in the reduced sample compared to that of the reoxidized sample. The counts of lattice oxygen OI were significantly lower in the 5VCe sample than that in the 1VCe sample, which suggests a high extent of oxygen removal in the V-saturated ceria lattice. However, the high OII and OIII areas were related to poor oxygen recovery in the 5VCe sample after reoxidation. It can be inferred that the saturated vanadium ions impede oxygen transport into the ceria lattice. However, longer oxidation cycles helped in improving the oxygen exchange and cycle capacity.

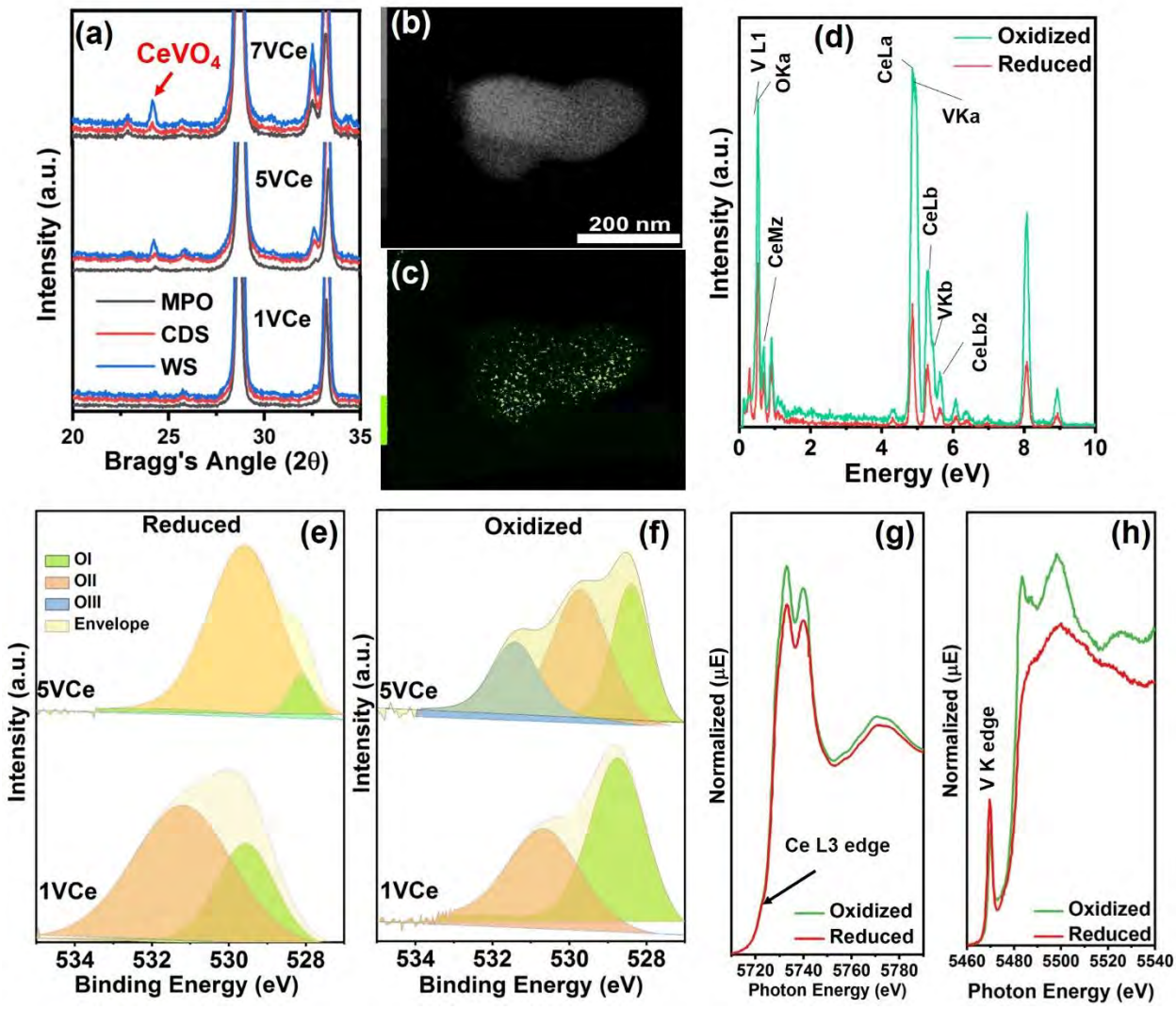

Figure 10. Structural study of cycled *x*VCeO$_2$ samples: (a) XRD patterns of cycled *x*VCeO$_2$ with 1, 5 and 7% vanadium. Information about the CeVO$_4$ phase evaluation after reduction, CO$_2$ splitting and water splitting reaction is shown from 20°–35°. (b) Grey scale and (c) green (carbon) STEM-EDS maps and (d) EDS spectra of 5VCeO$_2$ powders after the redox reactions. XPS O 1s spectra of *x*VCeO$_2$ samples after (e) reduction and (f) re-oxidation reactions with different areas of OI, OII and OIII peaks. XANES spectra of (g) Ce L3 and (h) V K edges of 5VCeO$_2$ samples after reduction and re-oxidation reactions.

Ex-situ XANES analysis revealed the chemical states of Ce and V elements after the redox reactions (Figures 10g and 10h). The photon energy of the Ce L3-edge remained unchanged at 5727eV. The post-edge features of the Ce L3 and V K edges showed lower intensity counts due to

the oxygen vacancy created after reduction. In addition, absorption of the V K-edge shifted to lower photon energies in the reduced samples when compared to that of the oxidized sample.

Stability of the V-doped ceria sample is demonstrated by performing 200 continuous S/MPO–CDS redox cycles. An expected initial decline in the syngas production rates was observed, which may be due to incomplete oxygen recovery (Figure 11a). On average, H_2 and CO were produced at a rate of 1.94 mmol min^{-1} g^{-1} and 0.91 mmol min^{-1} g^{-1}, respectively, during the MPO reaction. The CO production rates by CO_2 splitting were nearly equal to those produced during the MPO reaction. Figure 11b shows an expanded view of the syngas production rates from the 30^{th} to the 35^{th} cycle of the stability test. Average yields of H_2 and CO produced in the reduction step were 3.1 mmol g^{-1} and 1.37 mmol g^{-1}, respectively, and the oxidation of the samples produced up to 0.89 mmol g^{-1} of CO on average (Figure 11c). The surface analysis revealed that the counts of OI on after cycled $1VCeO_2$ powder surfaces were lower than with the pristine sample, which also relates to the incomplete oxygen recovery by the lattice (Figure 11d). However, surface carbon species may also be the reason for the low oxygen signal. Repeated oxygen exchange pulls the vanadium atoms from the ceria lattice to the surface during the 200-cycle test, which can be observed in the V 2P spectrum measured on after-cycled powder surfaces (Figure 11e).

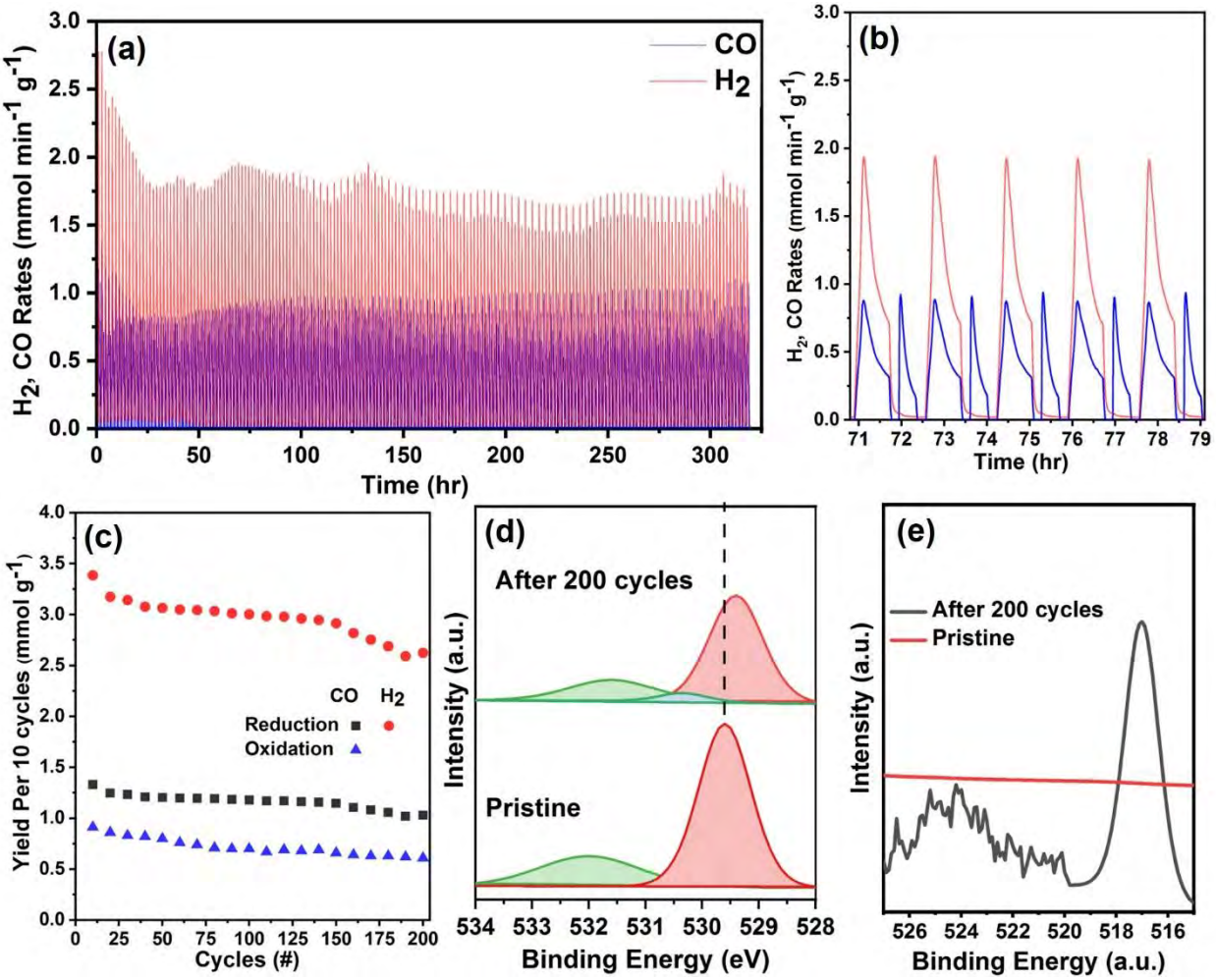

Figure 11. Thermochemical redox stability test of 1VCeO$_2$ powders: (a) syngas production rates, (b) expanded view of production rates for 5 cycles and (c) syngas yields produced during 200 S/MPO–CDS redox cycles. XPS (d) O1s and (e) V 2P spectra of pristine and after cycled 1VCeO$_2$ powders.

IV. Discussion

The structural data acquired by XRD, XPS, TEM and XANES suggests three stages of vanadium incorporation into the ceria lattice: (1) pre saturation (1–3%V), (2) saturation (5%V), and (3) post saturation (>5%V), as shown in Figure 12. The lattice spacing increases in stage 1 due to the lattice distortions caused by the mismatch in cationic radii. The expanded lattice along with the +5-oxidation state of vanadium create more oxygen vacancies and facilitate the oxygen transport and results in an efficient oxidation of methane. According to the phase quantification data, high

concentrations of vanadium promote the formation of $CeVO_4$ by impeding the oxygen flow in the ceria lattice. The syngas rates and yield data acquired during the thermochemical performance testing also confirms low oxygen exchange in 5VCe sample during the reduction and oxidation cycles, while lattice oxygen in 1VCe is almost double that of vacancy oxygen, which points to an efficient oxygen recovery due to easy oxygen flow. The segregation of $CeVO_4$ on CeO_2 particles is achieved in the post-saturation stage of vanadium doping, which greatly influences the redox performance of ceria.

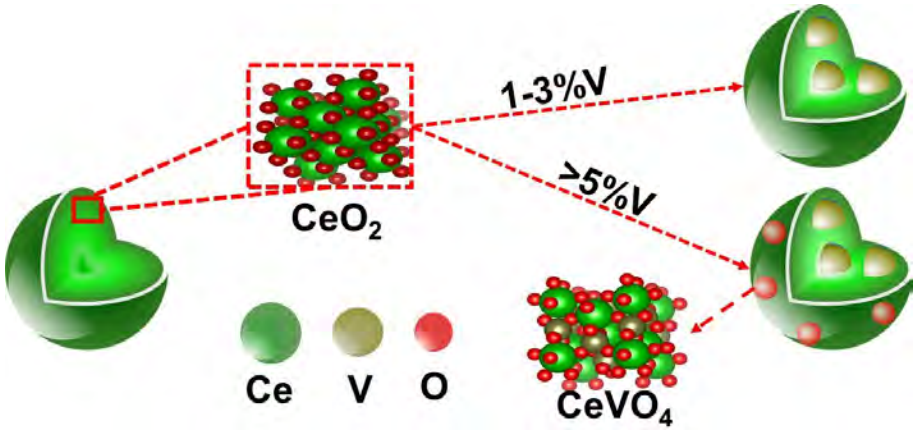

Figure 12. Proposed mechanism of vanadium doping into the ceria structure.

Cyclic $CeVO_4$ formation with high V-contents pushes the vanadium ions onto the powder surface and cause methane cracking and CO_2 poisoning. High H_2/CO ratios and deposited carbon verify this statement in V-rich *x*VCe samples during MPO–CDS cycles, when compared to that of MPO–WS redox cycles. Pure $CeVO_4$ powders show similar result, where considerable amounts of CO during the H_2O splitting reaction indicate the oxidation of carbon deposited onto the powder surface. This indicates that existence of the separate CeO_2 phase contributes to impeding the methane cracking via its high ionic conductivities, whereas the vanadium ions present onto the powder surface promote the cracking of methane and produce solid carbon. Here, the doping concentration of vanadium must be controlled to avoid the formation of $CeVO_4$ in the V-doped

CeO_2 nanostructures. However, the role of $CeVO_4$ is entirely different in the CeO_2-$CeVO_4$ "mixed-phase" systems, as reported in our previous study.[10] Based on the before and after cycling XPS analysis and the syngas yields data, we hypothesize that vanadium situated in the lattice improves the cycle capacity of ceria by providing reducing sites for methane, whereas surface vanadium actively participates in the redox reactions and results in high carbon contents and low fuel purity.

The duration of the redox reactions also plays a significant role in the rates of methane partial oxidation and CO_2/H_2O splitting cycles. The after-cycling XPS analysis of V-doped CeO_2 nanopowders confirms the migration of saturated vanadium atoms from the lattice to the surface of ceria particles during long reductions. Whereas, short reduction reactions produce less carbon content and the H_2/CO ratios are controlled, which is not the case in long redox cycles. The oxygen exchange in the V-saturated *x*$VCeO_2$ powders also improves during the L/MPO–CDS redox cycles due to long reduction durations at high temperatures.

The nature of the oxidation atmosphere displays a critical effect on material behavior and the chemistry of redox reactions. The carbonaceous atmosphere drastically increases the H_2/CO ratios and produces more carbon deposits compared to that from the H_2O splitting reactions, which can be verified from figures 7, 8 and 9. The oxidation of surface carbon species greatly influences the regeneration of $CeVO_4$ phase by suppressing the oxygen transfer, which can be avoided by optimizing the CH_4 and CO_2 flow rates.

V. Conclusions

This study demonstrates the successful doping of vanadium into ceria structures to produce syngas via solar-driven thermochemical redox cycles. Different doping concentrations were strategically incorporated to investigate the saturation limit of vanadium into the ceria structures. This helped

to evaluate the role of vanadium in the enhancement of syngas production rates and yields when it is present in the lattice and on the surface of ceria. Vanadium situated inside the ceria lattice simply increased the cycle capacity of ceria by facilitating the oxygen exchange in the expanded lattice and the surface vanadium reacted with CeO_2 and form a separate $CeVO_4$ phase. This segregated phase took part in the partial oxidation of methane by exchanging ½ of its O_2 molecule. The activation temperature for an efficient methane partial oxidation reaction decreased from 962°C in pure ceria to 784°C in V-doped ceria. The syngas production yields also increased by 200–400% with stable rates, after the vanadium doping. A long-term stability test produced up to 90 mmol g^{-1} of total syngas during 200 cycles of CO_2 splitting reactions. During these consecutive cycles, V-doped ceria exhibits continuous release of oxygen during the reduction reactions and efficiently draws oxygen from CO_2 upon reoxidation. The XPS study revealed that some vanadium escapes the lattice and accumulates on the surface of ceria powders due to the repetitive exchange of oxygen. However, low vanadium contents (below the saturation levels) on the surface do not react with ceria. X-ray diffraction reveals that the carbonaceous environments promote the vanadium and ceria reactions when compared to H_2O. This demonstration of V-doped ceria in thermochemical redox cycles, leaves significant room for improvement and may lead to the design of new oxygen carriers and catalysts, which will result in the desired thermochemical performance.

Acknowledgements

This project was supported by the Australian Research Council (ARC Future Fellowship FT140101213 by W. Lipiński). This study used the facilities and the scientific and technical assistance at the Centre of Advanced Microscopy at the Australian National University. We are grateful to Colin Carvolth and Kevin Carvolth for their assistance with setting up the IR furnace

experiments. Asim Riaz would especially acknowledge his beloved wife Sijia Tao for her moral support.

Author contribution

A. Riaz conceived the idea of utilizing V-doped ceria metal oxides for syngas production and conducted the experiments. A. Riaz wrote the manuscript with the professional guidance of A. Lowe and W. Lipiński. A. Riaz, T. Tsuzuki, A. Lowe and W. Lipiński contributed to the discussion and revisions of the manuscript. F. Kremer, T. Kim and S. Sattayaporn performed and processed the HRTEM/STEM, EELS and Synchrotron XAS analysis of materials, respectively.

Declaration of interests

The authors declare no competing financial interests.

References

[1] G.D. Scholes, G.R. Fleming, A. Olaya-Castro, R. Van Grondelle, Lessons from nature about solar light harvesting, Nat. Chem. 3 (2011) 763–774. https://doi.org/10.1038/nchem.1145.

[2] R.J. Carrillo, J.R. Scheffe, Advances and trends in redox materials for solar thermochemical fuel production, Sol. Energy. 156 (2017) 3–20. https://doi.org/10.1016/j.solener.2017.05.032.

[3] A. Steinfeld, Solar thermochemical production of hydrogen–a review, Sol. Energy. 78 (2005) 603–615. https://doi.org/10.1016/j.solener.2003.12.012.

[4] R. Bader, W. Lipiński, Solar Thermal Processing, in: M.J. Blanco, L.R. Santigosa (Eds.), Advances in Concentrating Solar Thermal Research Technology, 1st ed., woodhead

publishing, Amsterdam, 2017: pp. 403–459. https://doi.org/https://doi.org/10.1016/B978-0-08-100516-3.04001-6.

[5] M. Romero, A. Steinfeld, Concentrating solar thermal power and thermochemical fuels, Energy Environ. Sci. 5 (2012) 9234–9245. https://doi.org/10.1039/c2ee21275g.

[6] C.L. Muhich, B.D. Ehrhart, I. Al-shankiti, B.J. Ward, C.B. Musgrave, A.W. Weimer, A review and perspective of efficient hydrogen generation via solar thermal water splitting, Wiley Interdiscip. Rev. Energy Environ. 5 (2016) 261–287. https://doi.org/10.1002/wene.174.

[7] A. Steinfeld, P. Kuhn, J. Karni, High-temperature solar thermochemistry: Production of iron and synthesis gas by Fe_3O_4-reduction with methane, Energy. 18 (1993) 239–249. https://doi.org/10.1016/0360-5442(93)90108-P.

[8] X. Gao, I. Di Bernardo, P.B. Kreider, T. Tran-phu, X. Cai, N. Wang, J. Lipton-duffin, A. Bayon, W. Lipiński, A. Tricoli, Lattice Expansion in Optimally-Doped Manganese Oxide : An Effective Structural Parameter for Enhanced Thermochemical Water Splitting, ACS Catal. 9 (2019) 9880–9890. https://doi.org/10.1021/acscatal.9b03205.

[9] D. Arifin, A. Ambrosini, S.A. Wilson, B. Mandal, C.L. Muhich, A.W. Weimer, Investigation of Zr, Gd/Zr, and Pr/Zr – doped ceria for the redox splitting of water, Int. J. Hydrogen Energy. 45 (2020) 160–174. https://doi.org/10.1016/j.ijhydene.2019.10.177.

[10] A. Riaz, M.U. Ali, W. Lipiński, A. Lowe, Enhanced oxygen exchange capacity in nano-structured vanadia–ceria multi-phase oxygen carriers for solar thermal fuel production, J. Mater. Chem. A. 7 (2019) 27347–27360. https://doi.org/10.1039/C9TA06471K.

[11] P. Zhang, H. Lu, Y. Zhou, L. Zhang, Z. Wu, S. Yang, H. Shi, Q. Zhu, Y. Chen, S. Dai, Mesoporous $MnCeO_x$ solid solutions for low temperature and selective oxidation of hydrocarbons, Nat. Commun. 6 (2015) 8446. https://doi.org/10.1038/ncomms9446.

[12] S. Li, V.M. Wheeler, P.B. Kreider, R. Bader, W. Lipiński, Thermodynamic Analyses of Fuel Production via Solar-Driven Non-stoichiometric Metal Oxide Redox Cycling. Part 2. Impact of Solid-Gas Flow Configurations and Active Material Composition on System-Level Efficiency, Energy and Fuels. 32 (2018) 10848–10863. https://doi.org/10.1021/acs.energyfuels.8b02082.

[13] S. Li, P.B. Kreider, V.M. Wheeler, W. Lipiński, Thermodynamic Analyses of Fuel Production Via Solar-Driven Ceria-Based Nonstoichiometric Redox Cycling: A Case Study of the Isothermal Membrane Reactor System, J. Sol. Energy Eng. 141 (2019) 021012. https://doi.org/10.1115/1.4042228.

[14] B. Bulfin, J. Vieten, C. Agrafiotis, M. Roeb, C. Sattler, Applications and limitations of two step metal oxide thermochemical redox cycles; A review, J. Mater. Chem. A. 5 (2017) 18951–18966. https://doi.org/10.1039/c7ta05025a.

[15] W.C. Chueh, C. Falter, M. Abbott, D. Scipio, P. Furler, S.M. Haile, A. Steinfeld, High-Flux Solar-Driven Thermochemical Dissociation of CO_2 and H_2O Using Nonstoichiometric Ceria, Science. 330 (2010) 1797–1801. https://doi.org/10.1126/science.1197834.

[16] M.M. Nair, S. Abanades, Tailoring Hybrid Nonstoichiometric Ceria Redox Cycle for Combined Solar Methane Reforming and Thermochemical Conversion of H_2O/CO_2, Energy Fuels. 30 (2016) 6050–6058. https://doi.org/10.1021/acs.energyfuels.6b01063.

[17] A. Le Gal, S. Abanades, Dopant incorporation in ceria for enhanced water-splitting activity during solar thermochemical hydrogen generation, J. Phys. Chem. C. 116 (2012) 13516–13523. https://doi.org/10.1021/jp302146c.

[18] N. Gokon, T. Suda, T. Kodama, Thermochemical reactivity of 5-15 mol% Fe, Co, Ni, Mn-doped cerium oxides in two-step water-splitting cycle for solar hydrogen production, Thermochim. Acta. 617 (2015) 179–190. https://doi.org/10.1016/j.tca.2015.08.036.

[19] Z. Zhao, M. Uddi, N. Tsvetkov, B. Yildiz, A.F. Ghoniem, Redox Kinetics and Nonstoichiometry of $Ce_{0.5}Zr_{0.5}O_{2-\delta}$ for Water Splitting and Hydrogen Production, J. Phys. Chem. C. 121 (2017) 11055–11068. https://doi.org/10.1021/acs.jpcc.7b00644.

[20] F. Call, M. Roeb, M. Schmücker, C. Sattler, R. Pitz Paal, R. Pitz-Paal, R. Pitz Paal, Ceria doped with zirconium and lanthanide oxides to enhance solar thermochemical production of fuels, J. Phys. Chem. C. 119 (2015) 6929–6938. https://doi.org/10.1021/jp508959y.

[21] A. Riaz, M.U. Ali, T.G. Enge, T. Tsuzuki, A. Lowe, W. Lipiński, Concentration-Dependent Solar Thermochemical CO_2 /H_2O Splitting Performance by Vanadia–Ceria Multiphase Metal Oxide Systems, Research. 2020 *No*. 3049534. https://doi.org/10.34133/2020/3049534.

[22] Y. Zheng, X. Zhu, H. Wang, K. Li, Y. Wang, Y. Wei, Characteristic of macroporous CeO_2–ZrO_2 oxygen carrier for chemical-looping steam methane reforming, J. Rare Earths. 32 (2014) 842–848. https://doi.org/10.1016/S1002-0721(14)60151-4.

[23] Y. Zheng, K. Li, H. Wang, D. Tian, Y. Wang, X. Zhu, Y. Wei, M. Zheng, Y. Luo, Designed oxygen carriers from macroporous $LaFeO_3$-supported CeO_2 for chemical-looping reforming of methane, Appl. Catal. B Environ. 202 (2017) 51–63.

https://doi.org/10.1016/j.apcatb.2016.08.024.

[24] Z.H.U. Xing, W. Hua, W.E.I. Yonggang, L.I. Kongzhai, C. Xianming, X. Zhu, H. Wang, Y. Wei, K. Li, X. Cheng, Hydrogen and syngas production from two-step steam reforming of methane over CeO_2-Fe_2O_3 oxygen carrier, J. Rare Earths. 28 (2010) 907–913. https://doi.org/10.1016/S1002-0721(09)60225-8.

[25] D.R. Barcellos, F.G. Coury, A. Emery, M. Sanders, J. Tong, A. McDaniel, C. Wolverton, M. Kaufman, R. O'Hayre, Phase Identification of the Layered Perovskite $Ce_xSr_{2-x}MnO_4$ and Application for Solar Thermochemical Water Splitting, Inorg. Chem. 58 (2019) 7705–7714. https://doi.org/10.1021/acs.inorgchem.8b03487.

[26] A. Riaz, P. Kreider, F. Kremer, H. Tabassum, J.S. Yeoh, W. Lipiński, A. Lowe, Electrospun Manganese-Based Perovskites as Efficient Oxygen Exchange Redox Materials for Improved Solar Thermochemical CO_2 Splitting, ACS Appl. Energy Mater. (2019) acsaem.8b01994. https://doi.org/10.1021/acsaem.8b01994.

[27] A. Mishra, N. Galinsky, F. He, E.E. Santiso, F. Li, Perovskite-structured AMn: $XB_{1-x}O_3$ (A = Ca or Ba; B = Fe or Ni) redox catalysts for partial oxidation of methane, Catal. Sci. Technol. 6 (2016) 4535–4544. https://doi.org/10.1039/c5cy02186c.

[28] C. Huang, J. Wu, Y.T. Chen, M. Tian, A.I. Rykov, B. Hou, J. Lin, C.R. Chang, X. Pan, J. Wang, A. Wang, X. Wang, In situ encapsulation of iron(0) for solar thermochemical syngas production over iron-based perovskite material, Commun. Chem. 1 (2018) 2–11. https://doi.org/10.1038/s42004-018-0050-y.

[29] A.J. Carrillo, A.H. Bork, T. Moser, E. Sediva, Z.D. Hood, J.L.M.M. Rupp, Modifying $La_{0.6}Sr_{0.4}MnO_3$ Perovskites with Cr Incorporation for Fast Isothermal CO_2-Splitting

Kinetics in Solar-Driven Thermochemical Cycles, Adv. Energy Mater. 9 (2019) 1–13. https://doi.org/10.1002/aenm.201803886.

[30] Y. Zhu, N. Jin, R. Liu, X. Sun, L. Bai, H. Tian, X. Ma, X. Wang, Bimetallic $BaFe_2MAl_9O_{19}$ (M = Mn, Ni, and Co) hexaaluminates as oxygen carriers for chemical looping dry reforming of methane, Appl. Energy. 258 (2020) 114070. https://doi.org/10.1016/j.apenergy.2019.114070.

[31] S. Isarapakdeetham, P. Kim-Lohsoontorn, S. Wongsakulphasatch, W. Kiatkittipong, N. Laosiripojana, J. Gong, S. Assabumrungrat, Hydrogen production via chemical looping steam reforming of ethanol by Ni-based oxygen carriers supported on CeO_2 and La_2O_3 promoted Al_2O_3, Int. J. Hydrogen Energy. 45 (2019) 1477–1491. https://doi.org/10.1016/j.ijhydene.2019.11.077.

[32] C. Lu, K. Li, X. Zhu, Y. Wei, L. Li, M. Zheng, B. Fan, F. He, H. Wang, Improved activity of magnetite oxygen carrier for chemical looping steam reforming by ultrasonic treatment, Appl. Energy. 261 (2020) 114437. https://doi.org/10.1016/j.apenergy.2019.114437.

[33] D. Zeng, D. Cui, Y. Lv, Y. Qiu, M. Li, S. Zhang, R. Xiao, A mixed spinel oxygen carrier with both high reduction degree and redox stability for chemical looping H_2 production, Int. J. Hydrogen Energy. 45 (2019) 1444–1452. https://doi.org/10.1016/j.ijhydene.2019.11.062.

[34] Y.Y. Luo, D.S. Jo, K. Senthil, S. Tezuka, M. Kakihana, K. Toda, T. Masaki, D.H. Yoon, Synthesis of high efficient Ca_2SiO_4:Eu_2 green emitting phosphor by a liquid phase precursor method, J. Solid State Chem. 189 (2012) 68–74. https://doi.org/10.1016/j.jssc.2011.11.046.

[35] R. Sinclair, S.C. Lee, Y. Shi, W.C. Chueh, Structure and chemistry of epitaxial ceria thin films on yttria-stabilized zirconia substrates, studied by high resolution electron microscopy, Ultramicroscopy. 176 (2017) 200–211. https://doi.org/10.1016/j.ultramic.2017.03.015.

[36] D.S. Su, M. Wieske, E. Beckmann, A. Blume, G. Mestl, R. Schlögl, Electron beam induced reduction of V_2O_5 studied by analytical electron microscopy, Catal. Letters. 75 (2001) 81–86. https://doi.org/10.1023/A:1016754922933.

[37] V. Panchal, S. López-Moreno, D. Santamaría-Pérez, D. Errandonea, F.J. Manjón, P. Rodríguez-Hernandez, A. Muñoz, S.N. Achary, A.K. Tyagi, Zircon to monazite phase transition in $CeVO_4$: X-ray diffraction and Raman-scattering measurements, Phys. Rev. B - Condens. Matter Mater. Phys. 84 (2011) 1–12. https://doi.org/10.1103/PhysRevB.84.024111.

[38] Z. Wu, M. Li, S.H. Overbury, A Raman Spectroscopic Study of the Speciation of Vanadia Supported on Ceria Nanocrystals with Defined Surface Planes, ChemCatChem. 4 (2012) 1653–1661. https://doi.org/10.1002/cctc.201200243.

[39] Z. Wu, A.J. Rondinone, I.N. Ivanov, S.H. Overbury, Structure of Vanadium Oxide Supported on Ceria by Multiwavelength Raman Spectroscopy, J. Phys. Chem. C. 115 (2011) 25368–25378. https://doi.org/10.1021/jp2084605.

[40] M. V. Martínez-Huerta, J.M. Coronado, M. Fernández-García, A. Iglesias-Juez, G. Deo, J.L.G.G. Fierro, M.A. Bañares, Nature of the vanadia-ceria interface in V^{5+}/CeO_2 catalysts and its relevance for the solid-state reaction toward $CeVO_4$ and catalytic properties, J. Catal. 225 (2004) 240–248. https://doi.org/10.1016/j.jcat.2004.04.005.

[41] J. Mendialdua, R. Casanova A', Y. Barbaux, XPS studies of V_2O_5, V_6O_{13}, VO_2 and V_2O_3, J. Electron Spectros. Relat. Phenomena. 71 (1995) 249–261.

[42] Y.J. Park, N.G. Park, K.S. Ryu, S.H. Chang, S.C. Park, S.M. Yoon, D.K. Kim, RF-sputtered vanadium oxide thin films: Effect of oxygen partial pressure on structural and electrochemical properties, Bull. Korean Chem. Soc. 22 (2001) 1015–1018.

[43] M. V. Martínez-Huerta, G. Deo, J.L.G. Fierro, M.A. Bañares, Changes in ceria-supported vanadium oxide catalysts during the oxidative dehydrogenation of ethane and temperature-programmed treatments, J. Phys. Chem. C. 111 (2007) 18708–18714. https://doi.org/10.1021/jp0772225.

[44] J. Matta, D. Courcot, E. Abi-Aad, A. Aboukaïs, Identification of Vanadium Oxide Species and Trapped Single Electrons in Interaction with the $CeVO_4$ Phase in Vanadium−Cerium Oxide Systems. 51 V MAS NMR, EPR, Raman, and Thermal Analysis Studies, Chem. Mater. 14 (2002) 4118–4125. https://doi.org/10.1021/cm010396t.